Final Report on the ALMA Development Study "Calibration Refinements for ALMA Imaging"

I. S. Adams, K. Stewart, T. L. Wilson (Naval Research Laboratory, Washington, D.C. 20375)

I. Introduction

This is final report of the ALMA Development Study. This reviews the 3 previous study reports and suggests future development.

The general topic of atmospheric fluctuations which affect millimeter interferometers has been reviewed by M. Bremer in the proceedings of the IRAM Millimeter Interferometer Summer School (ed. A. Dutry), available for a download from the IRAM website. In the following sections, we review and update the previous reports in the study. The first two sections are short updates of previous reports; the third section contains new results from model calculations and satellite measurements of the AOS. A fourth section lists recommendations.

II. Group Delay

This refers to corrections to phase across a 2 GHz wide spectral window for correlations between pairs of near and distant antennas, at 237 GHz. The present ALMA calibration scheme is to correct phase across the entire band using an estimate from the output of Water Vapor Radiometers (WVRs). Using the data for the Orion KL source from the Commissioning & Science Verification (CSV) data set, we compared the *"non-dispersive"* Group Delay correction, that is, one value of delay per spectral window (now in use) with the *"dispersive delay"* Group Delay correction, in which the ATM model is used to apply frequency-dependent corrections on a channel-by-channel basis. This prototype analysis shows that the application of *"dispersive delay"* corrections is viable, but for the 237 GHz range, the differences between *"non-dispersive"* and *"dispersive"* corrections are not significant because of the choice of frequency. Since our investigation, R. Hills (unpublished memo of Sept. 29, 2014) had analyzed ALMA data for data at 358, 360 (both lower sideband), 371 and 372 GHz (upper sideband). The upper sideband is close to an atmospheric water vapor line. Hills' conclusion is that the correction from the ATM model is a factor of 2 too large. We are presently analyzing data for the asteroid Juno at 224, 226, 240 and 242 GHz, so an investigation of this conclusion must await our analysis of another dataset.

III. Self-Calibration at low Signal to Noise Ratios

As with the Group Delay study, this investigation made use of the Orion KL data from the CSV tests. These were more complex, but showed that the approach of Schwab & Cotton (1983) was promising. Briefly, this is a simultaneous solution for all antennas, searching for the best fit to delay and fringe rate parameters. This task is illustrated in Fig. 1 of Schwab & Cotton. The task is in the task FRINGE in AIPS, and the algorithms are in the Schwab & Cotton paper. That paper describes an optimization of the procedure. An implementation in CASA would have to be a cooperative effort with the CASA team at NRAO in Socorro.

IV. Extending ALMA Corrections with Remote Sensing Data

To investigate cloud properties and statistics at the ALMA array operations site (AOS), and to produce estimates of path delay due to liquid and ice clouds, we considered the CloudSat Radar-Visible Optical Depth Cloud Water Content (RVOD-CWC) product (Austin, 2001; Austin, 2008; Wood, 2008), which synergistically combines CloudSat CPR profiles with optical depth information from MODIS. As part of the A-Train constellation, and to produce high-quality combined products, CloudSat is kept in tight formation with a repeat ground track coming every 233 orbital revolutions (every 16 days). The ground track is such that CloudSat passes almost directly over the ALMA site twice in 16 days—once during an ascending node, once during a descending node. The ground track pattern can be seen in Figure 1, with the AOS denoted with a white circle. To determine site cloud cover and cloud microphysics, we limited the data we used to CloudSat profiles within 10 km of the AOS, yielding 526 profiles for the calendar year 2007. Of these profiles, 33.1% (174) contained either liquid or ice clouds. The presence of clouds should therefore be considered a major concern. Figure 2 shows the monthly water path totals for liquid, ice, and the combination of the two. January and June show large relative increases to the amount of cloud over the AOS.

Since the frequency range for ALMA is primarily in the scattering regime for larger cloud liquid droplets and, in particular, cloud ice particles, the Rayleigh approximation is not sufficient for calculating the refractivity of clouds. Instead the amplitude scattering matrix (Bohren and Huffman, 1983), which relates the parallel (ϑ) and perpendicular (φ) components of the scattered electric field to those of the incident electric field, must be calculated. Using the notation of Mishchenko (1990),

$$\begin{bmatrix} E_{\vartheta}^{\mathrm{sca}} \\ E_{\varphi}^{\mathrm{sca}} \end{bmatrix} = \frac{e^{ikR}}{R} \begin{bmatrix} S_{11} & S_{12} \\ S_{21} & S_{22} \end{bmatrix} \begin{bmatrix} E_{\vartheta}^{\mathrm{inc}} \\ E_{\varphi}^{\mathrm{inc}} \end{bmatrix}$$

Various methods are available for computing the amplitude scattering matrix, and one widely used approach for rotationally symmetric geometries is the T-Matrix (Waterman, 1971) which expands the incident and scattered electric fields as spherical wave functions. For spheres T-Matrix reduces to Lorenz-Mie theory. We used T-Matrix code for scatterers with fixed orientation (Mishchenko, 2000) to compute the scattering properties of liquid and ice spheres, as this code readily outputs the amplitude scattering matrix. For the complex permittivity of liquid and ice, which are needed for T-Matrix calculations, we used fits developed by Ellison (2007) and Mätzler (2006), respectively. From the amplitude scattering matrix elements, we then compute the delay (ρ) and extinction (k):

$$\rho = \frac{\lambda^2}{4\pi} \int_0^{\infty} N(x) Re\{S_{11} + S_{22}\} dx$$

$$k = \lambda \int_0^{\infty} N(x) Im\{S_{11} + S_{22}\} dx$$

where $N(x)$ is the size distribution of cloud water droplets in terms of droplet radius or the size distribution of ice particles in terms of particle diameter.

For the cloud model, we used the lognormal distribution utilized to retrieve RVOD-CWC products. For liquid clouds,

$$N(r) = \frac{N_T}{\sqrt{2\pi}\sigma r} e^{\frac{-\ln^2(r/r_g)}{2\sigma^2}}$$
$$r_e = r_g e^{\frac{5}{2}\sigma^2}$$

where N_T is the droplet number density, r is the droplet radius, r_g is the geometric mean radius, σ is the spread of the distribution, and r_e is the effective radius (the ratio of the third moment of the distribution to the second). Ice clouds are similarly defined:

$$N(D) = \frac{N_T}{\sqrt{2\pi}\sigma D} e^{\frac{-\ln^2(D/D_g)}{2\sigma^2}}$$
$$r_e = \frac{1}{2} D_g e^{\frac{5}{2}\sigma^2}$$

with diameter (D) replacing radius (r).

Based on the CloudSat statistics we computed mean hydrometeor effective radii ($\overline{r_e} = 13.6$ µm for liquid and $\overline{r_e} = 74.2$ µm for ice) and distribution width parameters ($\overline{\sigma}$ ~ 0.5 for both liquid and ice) from the 174 cloudy profiles. We then normalized the distributions such that the liquid and ice water contents were 1 mg m^{-3} (liquid water content over the AOS ranges from 0 to 1383 mg m^{-3} and ice water content ranges from 0 to 524 mg m^{-3}). Delay and extinction for liquid and ice clouds at three temperatures (0ºC, –20ºC, and –40ºC) are given in Figure 3, Figure 4, Figure 5, and Figure 6. The Rayleigh approximation is given in dashed lines to show that as frequency increases, the Rayleigh approximation rapidly diverges from the T-Matrix computations. Interestingly, while the complex permittivity of ice is nondispersive (Mätzler, 2006), scattering due to large ice crystals, though few in number, introduces a dispersive component to the path delay from ice. Also, while extinction from ice, particularly at lower frequencies, is rather low, the path delay is still appreciable. Extinction due to ice in the submillimeter wave range should be used carefully, as frozen hydrometeors in nature typically exhibit complex shapes, and solid geometries have been found to overestimate extinction when compared with higher-fidelity scattering calculations (Adams and Bettenhausen, 2012). For both liquid and ice, the nondispersive component of the path delay is the delay computed at ~0 GHz.

Based on the scattering and cloud model described above, we used the 174 cloudy profiles to calculate zenith path delays over the AOS. Temperature profiles, corresponding to the CloudSat profiles, were taken from the ECMWF-AUX product distributed at the CloudSat Data Processing Center. Examples for 100 GHz and 670 GHz are shown in Figure 6, Figure 8, Figure 9, and Figure 10. Path delay due to clouds is appreciable, and small changes in the amount of cloud in the path could exceed the path delay budget, particularly in the submillimeter range.

Given the large path delay contributions from clouds, and the fact that the presence of clouds will alter the relationship between 183 GHz brightness temperature and path delays for ALMA observing frequencies, we recommend comprehensive simulations to estimate the differential path delays for delay due to wet, dry, and cloud components using the available CloudSat data. The climatological study should also be broadened to properly characterize inter-seasonal variability and to determine inter-annual variability.

V. Recommendations for Future Work

Pursue the investigation of the corrections (based on WVR data) given by the ATM program.

Implement the Schwab-Cotton self-calibration scheme in CASA.

Install a small fish-eye lens optical camera to locate clouds over the whole sky at the site.

Incorporate the outputs of the Oxygen Sounding Thermal Profiler and Weather Stations at the AOS into the ASDM headers. These will aid in characterizing temperature versus elevation. Additional Oxygen Sounders would help to determine the scale and distribution of fluctuations.

Install GPS ground stations as a means to verify water vapor retrievals and wet path delay estimates. Incorporate the outputs in the ASDM headers.

Fund a project to fully characterize path delay (wet, dry, and clouds) and model differential delays. This can be done directly with CloudSat retrievals and auxiliary products.

References

Adams, I. S., and M. H. Bettenhausen (2012), The scattering properties of horizontally aligned snow crystals and crystal approximations at millimeter wavelengths, *Radio Sci.*, **47**, RS5007, doi:10.1029/2012RS005015

Austin, R. T., and G. L. Stephens (2001), Retrieval of stratus cloud microphysical parameters using millimeter-wave radar and visible optical depth in preparation for CloudSat, 1. Algorithm formulation, *J. Geophys. Res.*, **106**, D22, 28233–28242, doi:10.1029/2000JD000293

Austin, R. T., A. J. Heymsfield, and G. L. Stephens (2008), Retrieval of ice cloud microphysical parameters using the CloudSat millimeter-wave radar and temperature, *J. Geophys. Res.*, **114**, D8, doi:10.1029/2008JD010049

Bohren, C. F., and D. R. Huffman (1983), *Absorption and Scattering of Light by Small Particles*, John Wiley, New York

Ellison, W.J. (2007), Permittivity of pure water, at standard atmospheric pressure, over the frequency range 0–25 THz and the temperature range 0-100 ºC, *J. Phys. Chem. Ref. Data*, doi:10.1063/1.2360986

Mätzler, C. (2006), Microwave dielectric properties of ice, in *Thermal Microwave Radiation*: Applications for Remote Sensing, edited by C. Mätzler, pp. 455–462, Inst. of Eng. and Technol., London.

Mishchenko, M. I. (1990), Extinction of light by randomly-oriented non-spherical grains, *Astrophys. Space Sci.*, **164**, 1, 1–13, doi:10.1007/BF00653546

Mishchenko, M. I. (2000), Calculation of the amplitude matrix for a nonspherical particle in a fixed orientation. *Appl. Opt.*, **39**, 1026-1031, doi:10.1364/AO.39.001026

Schwab, F., Cotton, W. 1983 *Astronom. J.* 88, 688

Wood, N. (2008), Level 2B radar-visible optical depth cloud water content (2B-CWC-RVOD) process description document, CloudSat Project.

Waterman, P. C. (1971), Symmetry, unitarity, and geometry in electromagnetic scattering, *Phys. Rev. D*, **3**, 4, 825–839, doi:10.1103/PhysRevD.3.825

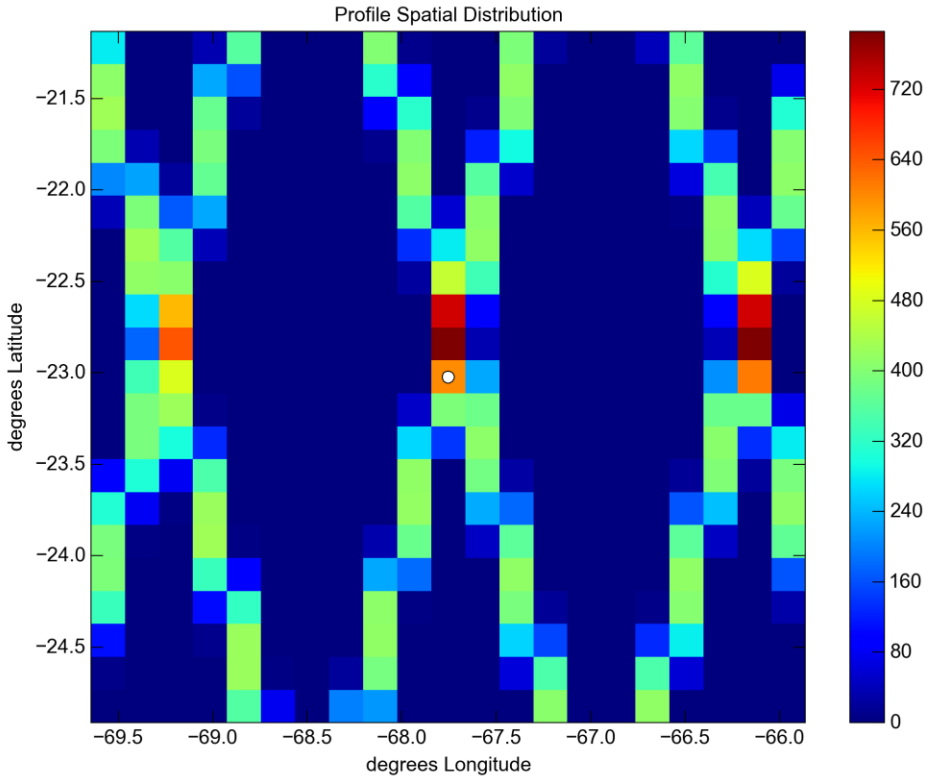

Figure 1: Absolute frequency of CloudSat observations over and around the AOS. The AOS is denoted with a white dot. The scale is to the right of this plot.

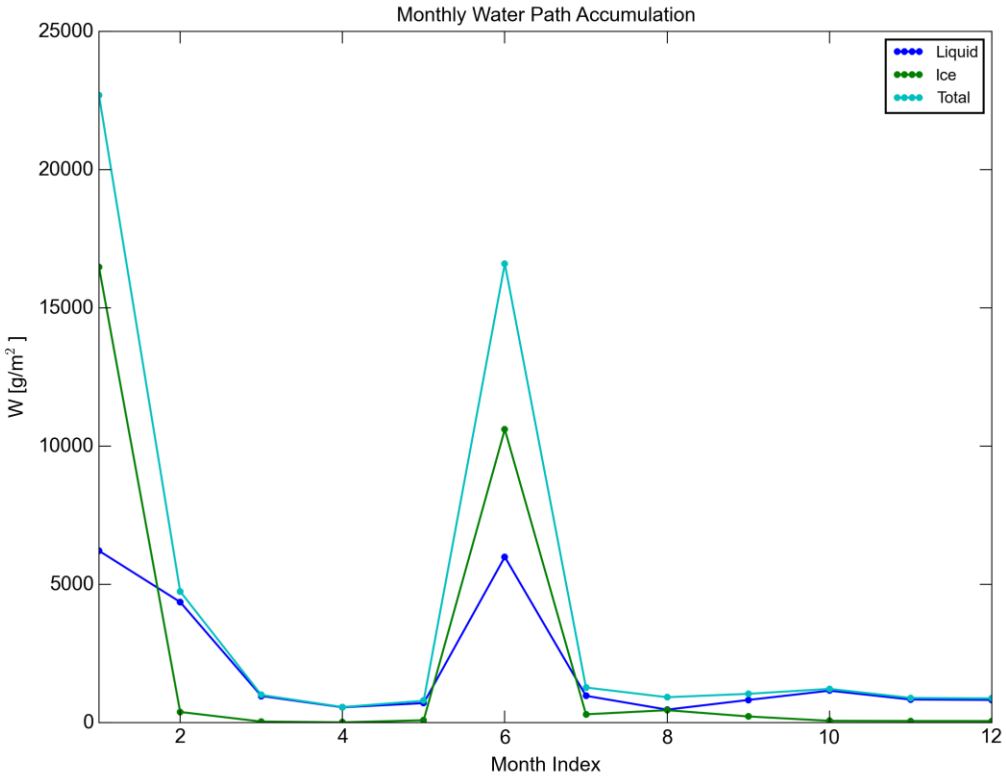

Figure 2: Monthly water path totals (1 kg m^{-2} is equivalent to 1mm of liquid water).

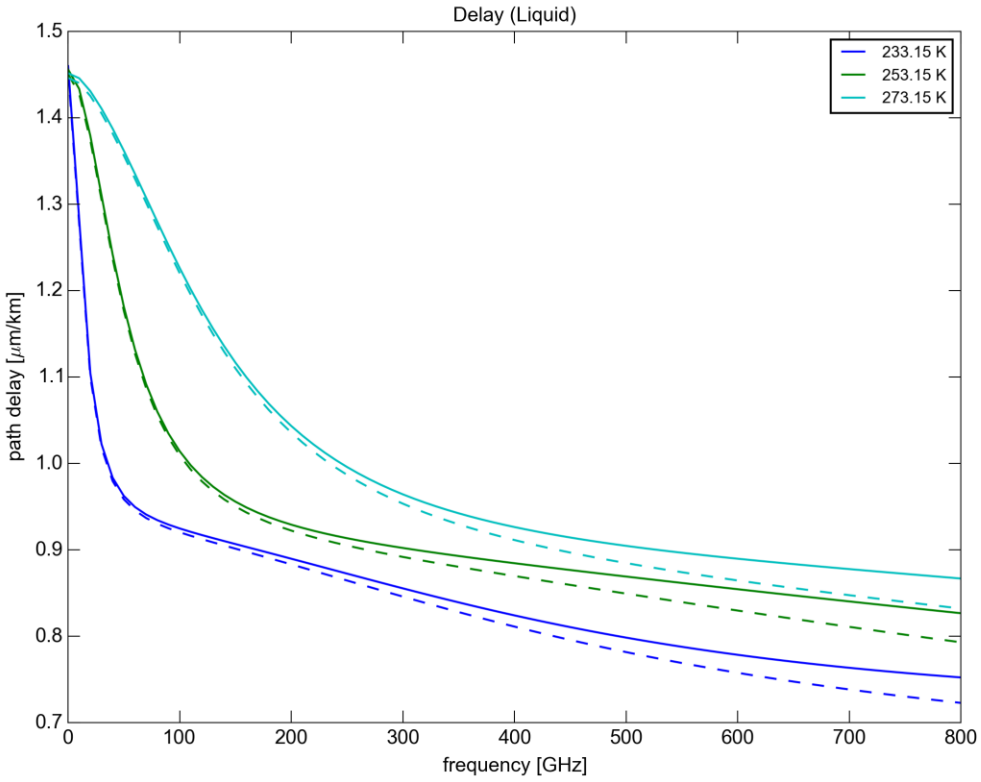

Figure 3: Delay for 1 mg m^{-3} of cloud liquid versus frequency for three temperatures. The Rayleigh approximation is displayed with dashed lines.

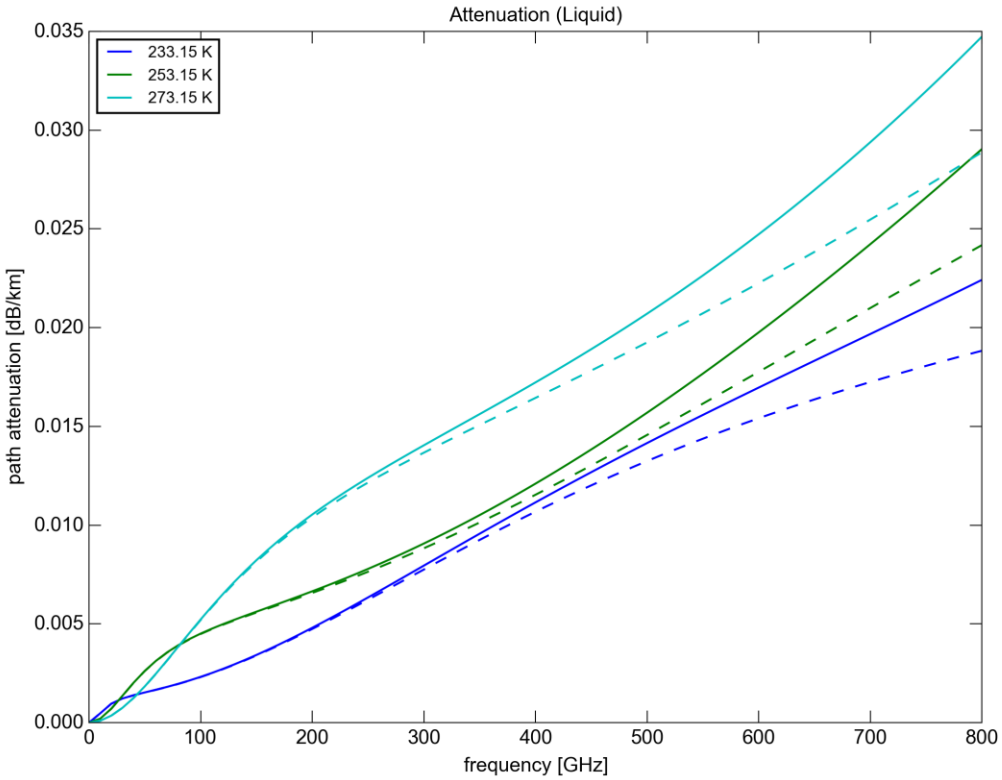

Figure 4: Extinction for 1 mg m^{-3} of cloud liquid versus frequency for three temperatures. The Rayleigh approximation is displayed with dashed lines.

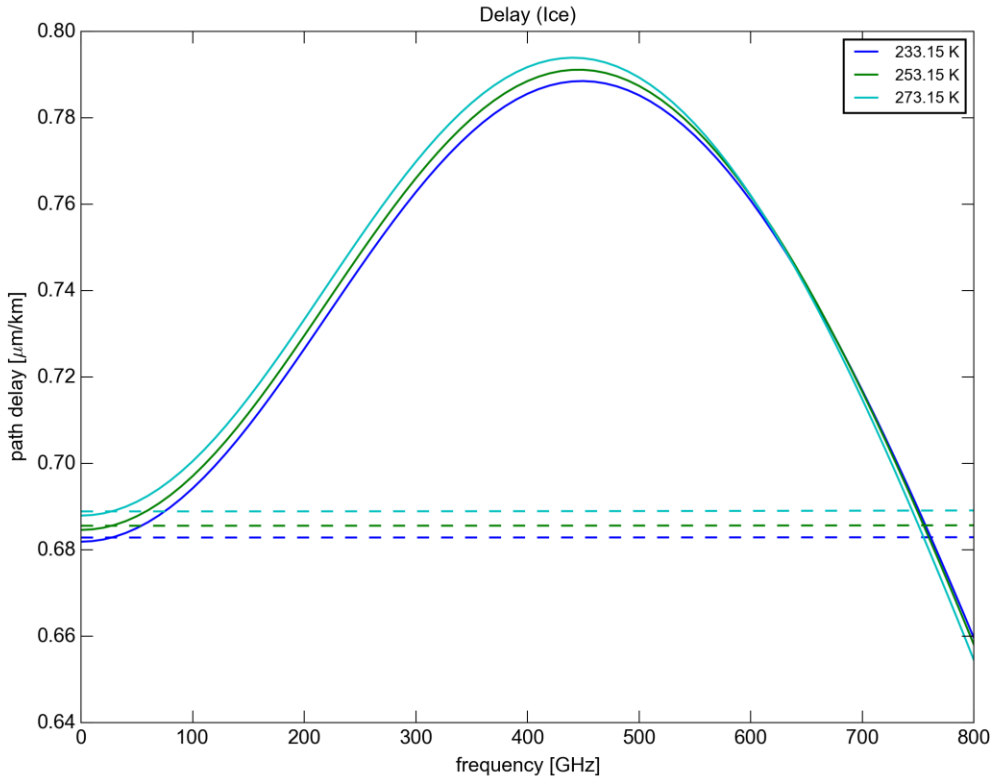

Figure 5: Delay for 1 mg m^{-3} of cloud ice versus frequency for three temperatures. The Rayleigh approximation is displayed with dashed lines.

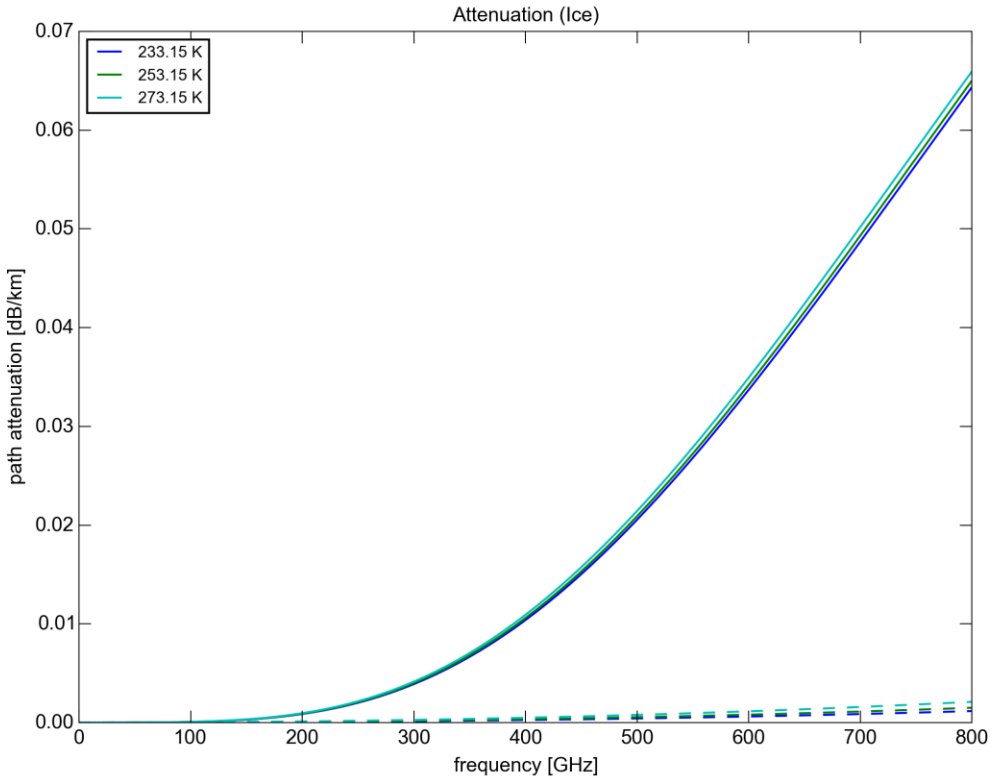

Figure 6: Extinction for 1 mg m^{-3} of cloud ice versus frequency for three temperatures. The Rayleigh approximation is displayed with dashed lines.

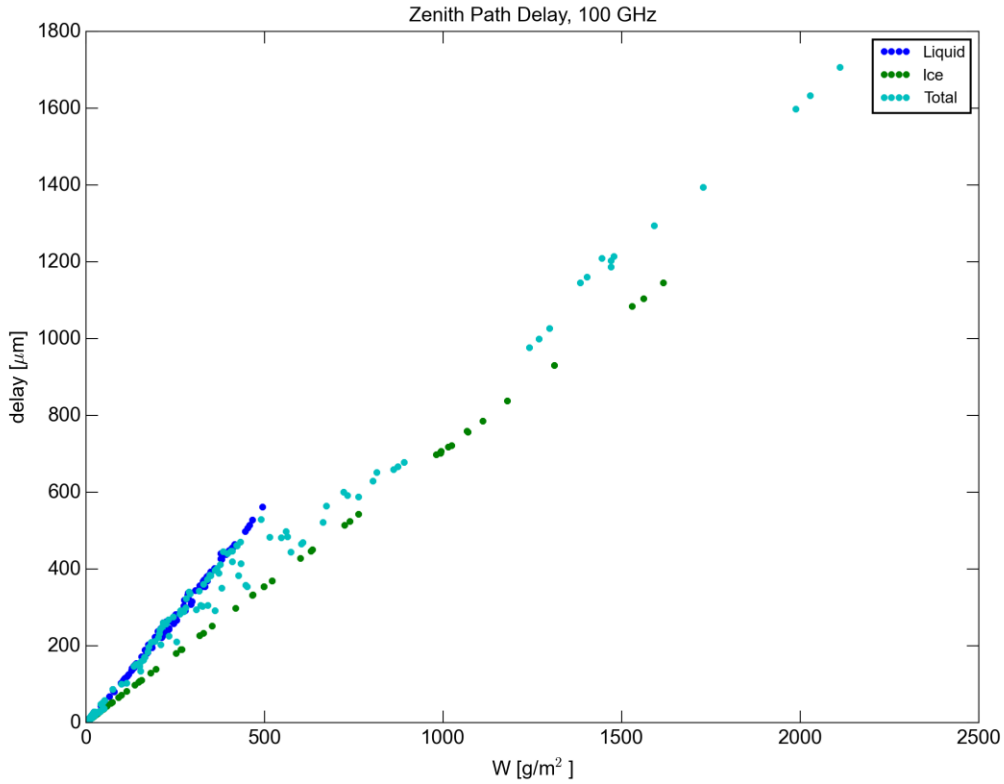

Figure 7: Computed zenith delay at 100 GHz for 174 cloudy profiles (1 kg m^{-2} is equivalent to 1mm of liquid water).

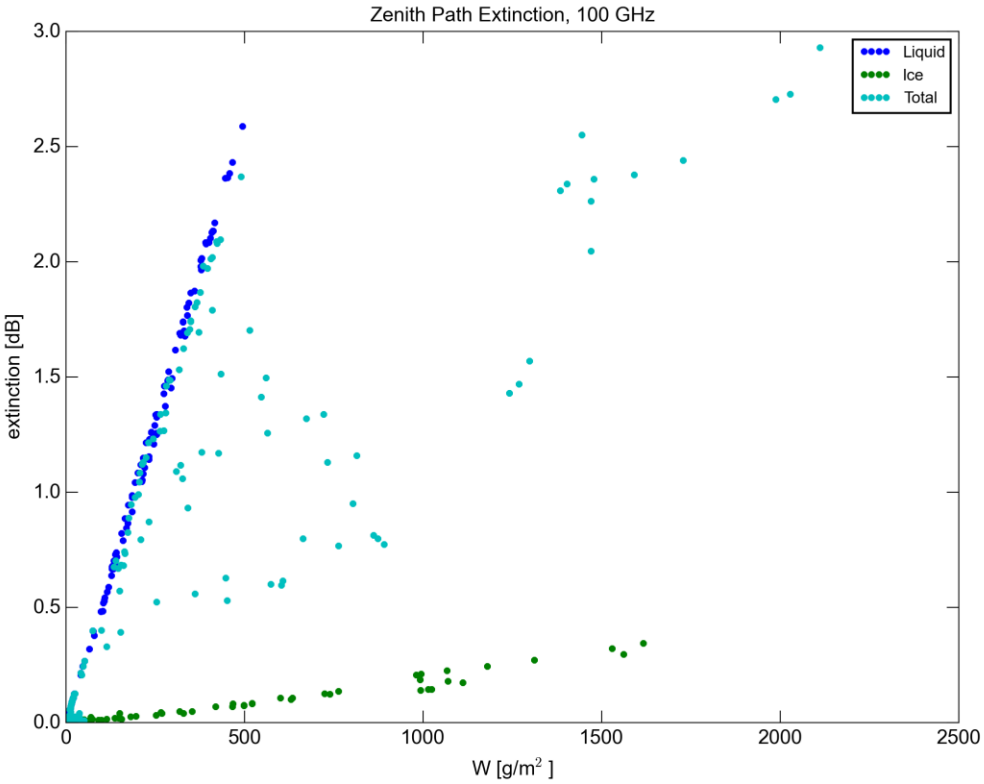

Figure 8: Computed zenith extinction at 100 GHz for 174 cloudy profiles (1 kg m^{-2} is equivalent to 1mm of liquid water).

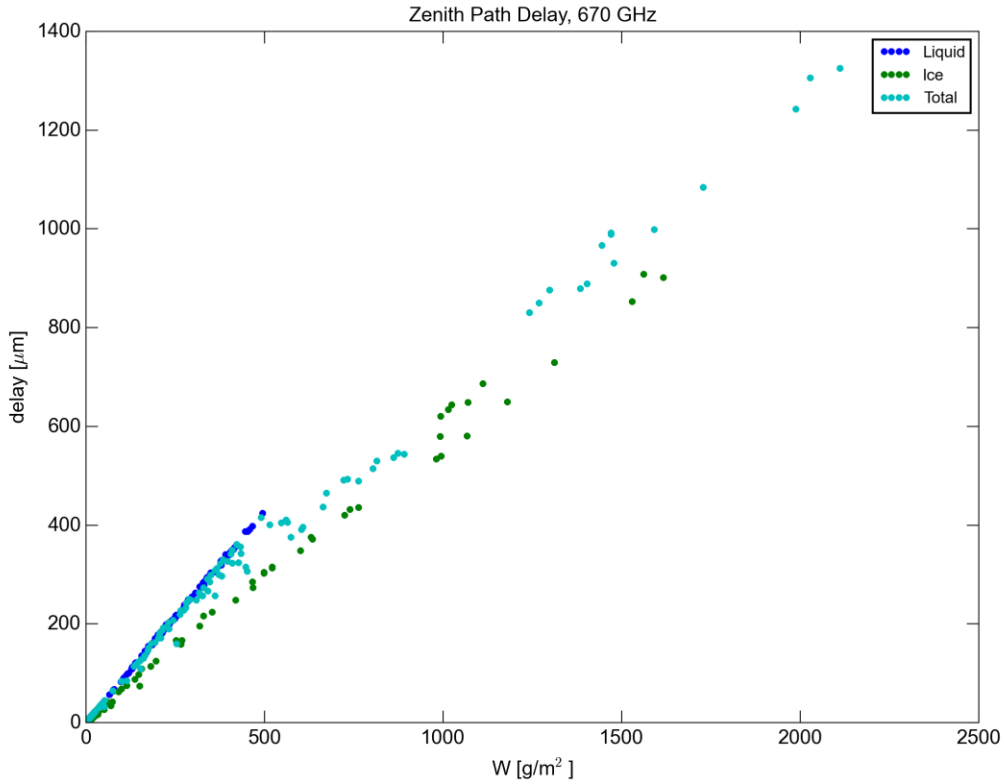

Figure 9: Computed zenith delay at 670 GHz for 174 cloudy profiles (1 kg m^{-2} is equivalent to 1mm of liquid water).

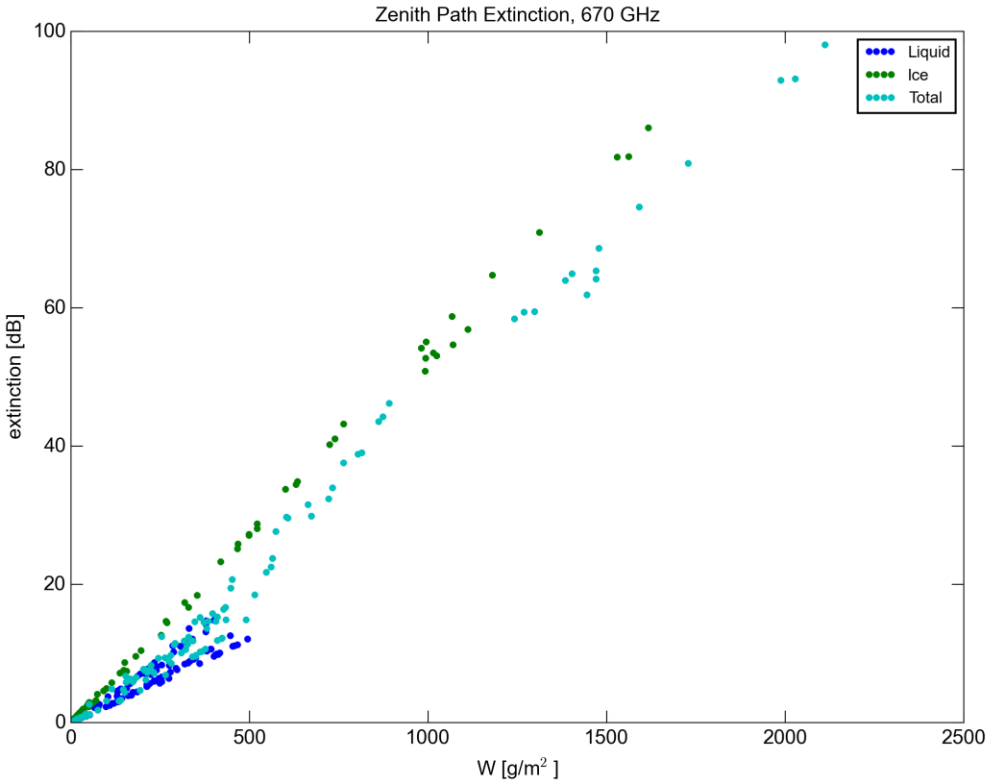

Figure 10: Computed zenith extinction at 670 GHz for 174 cloudy profiles (1 kg m^{-2} is equivalent to 1mm of liquid water).